THEORY OF ZEOLITE CATALYSIS

R. A. van Santen* and X. Rozanska

Schuit Institute of Catalysis, Eindhoven University of Technology
Eindhoven 5600 MB, The Netherlands

The reactivity of acidic zeolites to the activation of hydrocarbons is used to illustrate different modeling approaches applied to catalysis. Quantum-chemical calculations of transition-state and ground-state energies can be used to determine elementary rate constants. But to predict overall kinetics, quantum-mechanical studies have to be complemented with statistical methods to compute adsorption isotherms and diffusion constants as a function of micropore occupation. The relatively low turnover frequencies of zeolite-catalyzed reactions compared to superacid-catalyzed reactions are due mainly to high activation energies of the elementary rate constants of the proton-activated reactions. These high values are counteracted by the significant interaction energies of hydrocarbons with the zeolite micropore wall dominated by van der Waals interactions. © 2001 Academic Press.

*To whom correspondence should be addressed.

ADVANCES IN CHEMICAL ENGINEERING, VOL. 28 0065-2377/01 $35.00

I. Introduction

Predictability of activity, selectivity, and stability based on known structures of catalysts can be considered the main aim of the theoretical approaches applied to catalysis. Here, for a particular class of heterogeneous catalysts, namely, acidic zeolites, we present the theoretical approaches that are available to accomplish this goal, which lead to a better understanding of molecular motion within the zeolitic micropores and the reactivity of zeolitic protons. It is not our aim to introduce the methods as such, since introductory treatments on those can be found elsewhere. Rather we focus on their application and use to solve questions on mechanisms and reactivity in zeolites. The discussion is focused on an understanding of the kinetics of zeolite-catalyzed reactions.

We use the activation of linear alkanes and their conversion to isomers and cracked products as the main motive of our discussion. This class of reactions catalyzed by acidic zeolites is an ideal choice to illustrate the state of the art of theoretical molecular heterogeneous catalysis, because the reaction mechanisms, zeolite micropore structure, and structure of the catalytically reactive sites are rather well understood.

Whereas simulation methods are available to model zeolite structures as a function of their composition as well as their topology [1–9], we do not discuss

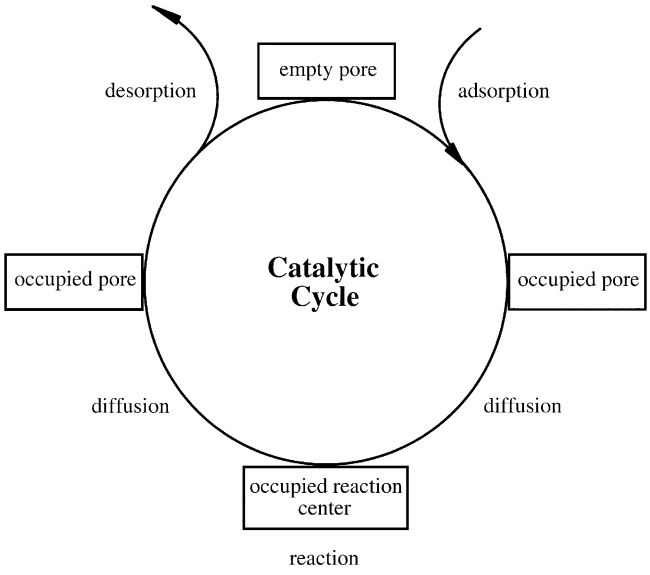

FIG. 1. The catalytic cycle of a zeolite-catalyzed reaction.

those techniques and their results here but refer to some of the results when discussing chemical reactivity and adsorption. Perpetual improvements in both computers and *ab initio* codes allow nowadays calculations on realistic structures [10–12]. Also, we do not present an overview of the deep mechanistic insights that have been obtained recently on a molecular level for many hydrocarbon conversion reactions. Most of the practically important reactions have now been analyzed by quantum-chemical techniques [13–31] (viz., reactions with aromatic species [13–16], olefins and alkanes [17–22], water and methanol [23–26], metallic clusters supported on zeolite or metal exchanged zeolites [27–30], and acetonitrile [31]).

We are concerned with the kinetics of zeolite-catalyzed reactions. Emphasis is put on the use of the results of simulation studies for the prediction of the overall kinetics of a heterogeneous catalytic reaction. As we will see later, whereas for an analysis of reactivity the results of mechanistic quantum-chemical studies are relevant, to study adsorption and diffusion, statistical mechanical techniques that are based on empirical potentials have to be used.

II. The Rate of a Catalytic Reaction

A catalytic reaction is the result of a cyclic process that consists of many elementary reaction steps. The essence of a catalytic reaction is that the catalytic reactive center reappears after each cycle in which reactant molecules are converted into products. Since zeolites are microporous systems, a special feature is the coupling of reaction at the protonic centers with diffusion of the molecules through the micropores to and from the zeolite exterior. The zeolite catalytic cycle is sketched in Fig. 1. To reach the catalytic reactive center, molecules have to adsorb in the mouth of a micropore and diffuse to the catalytic center, where they can react. Product molecules have to diffuse away and, once they reach the micropore mouth, will desorb. Clearly, then, one has to complement quantum-chemical information on reactivity, concerned with the interaction of zeolite protons with reactants, with information on diffusion and on adsorption of reactants and products.

Again, we do not exhaustively discuss molecular theories of diffusion and adsorption in zeolites but refer to other studies [32–34]. However, we highlight some important results significant to the kinetic analysis we are presenting.

A characteristic time scale of a catalytic reaction event such as proton-activated isomerization of an adsorbed alkene molecule is 10^2 s. However, quantum-chemical calculations predict energies of electrons with characteristic time scales of 10^{-16} s. Of use to us are the potential energies that such

methods generate that determine the forces that act on the nuclei, which determine the vibrational frequencies. The characteristic time of vibrational motion is 10^{-12} s. In zeolites, diffusional times can be as short as 10^{-8} s and adsorption time scales are typically 10^{-6} s. Dependent on the free energies of adsorption, the time scale of desorption of a molecule is 10^{-4} s or longer. The time scales of the proton-activated elementary reactions are of the order of 10^{-4} s due to their high activation energies. The long time scale of reaction compared to that of vibrational motion implies that thermal energy exchange between reaction molecule and zeolite wall is fast. This is the justification for the use of transition reaction rate theory [35–37]. In its most elementary form, the rate expression,

$$r_{\mathrm{TST}} = \frac{kT}{h}\, e^{(\Delta S\#/R)}\, e^{-(E_{\mathrm{act}}/RT)}, \tag{1}$$

can be shown to be rigorously valid, if the rate of energy exchange is fast. In Eq. (1), the probability of passing the activation energy barrier by reactants with sufficient energy has been assumed to be equal to one. In this equation, k is Boltzmann's constant, h is Planck's constant, $\Delta S\#$ is the activation entropy, and E_{act} is the transition state barrier height. R is the gas constant.

The major advance of the past decade is that, using quantum-chemical computations, activation energies (E_{act}) as well as activation entropies ($\Delta S\#$) can be predicted *a priori* for systems of catalytic interest. This implies much more reliable use of the transition-state reaction rate expression than before, since no assumption of the transition state-structure is necessary. This transition-state structure can now be predicted. However, the estimated absolute accuracy of computed transition states is approximately of the order of 20–30 kJ/mol. Here, we do not provide an extensive introduction to modern quantum-chemical theory that has led to this state of affairs: excellent introductions can be found elsewhere [38, 39]. Instead, we use the results of these techniques to provide structural and energetic information on catalytic intermediates and transition states.

Because of the size of the reaction centers to be considered, a breakthrough in quantum chemistry had been necessary to make computational studies feasible on systems of catalytic interest. This breakthrough has been provided by density functional theory (DFT). Whereas in Hartree–Fock-based methods, used mainly before the introduction of DFT, electron exchange had to be accounted for by computation of integrals that contain products of four occupied orbitals, in DFT these integrals are replaced by functionals that depend only on the electron density. An exchange-correlation functional can be defined that accounts for exchange as well as correlation energy. The correlation energy is the error made in Hartree–Fock-type theories by the use of the mean-field approximation for electronic motion.

The still unresolved problem is the determination of a rigorously exact functional, as all currently used DFT functionals are approximate.

By computation of the stationary points of the n-dimensional energy diagram of the interacting system, the structure of local energy minima as well as the transition state can be determined. For many systems, these interaction energies have an accuracy of the order of 5–15 kJ/mol. For this reason, as we illustrate later, discrepancies between theoretical calculation and experiment can be often related to shortcomings in model assumptions rather than to quantum-chemical approximations. Around the ground-state energy minimum and the transition-state saddle point, the potential can be expanded as a function of displacement of the normal coordinates with respect to their stationary values. Within the harmonic approximation, the vibrational spectrum and hence the corresponding entropy can be easily computed. The entropy follows from the expression

$$S = -k \ln pf \tag{2a}$$

$$= -k \ln \Pi_i \frac{1}{1 - e^{-(h\nu_i/kT)}}, \tag{2b}$$

where i sums over the n normal vibration modes of the ground-state system and the $n - 1$ normal modes of the transition state. pf stands for the partition function and ν_i is the normal mode frequency.

III. Zeolites as Solid Acid Catalysts

The structure of a zeolite is illustrated in Fig. 2, using mordenite as an example. The zeolitic framework can consist of four valent (Si), three valent (Al, Ga, Fe), or five valent (P) cations, tetrahedrally coordinated with four oxygen atoms. The oxygen atoms bridge two framework cations. When the lattice cation is Si^{+IV}, the framework charge is neutral. When Al^{+III} substitutes for Si^{+IV}, the framework becomes negatively charged. Zeolites of such a composition can exist when extra framework cations are ion exchanged into the zeolite cavities. In the case where this cation is NH_4^+, the heating of the material induces ammonia to desorb. The proton that is left behind will bind to an oxygen atom bridging Al and Si framework cations (see Fig. 3). For an extensive discussion of zeolite crystals of catalytic interest, refer to Refs. 40 and 41. Also, several available reviews discuss the nature of the proton bonded to the bridging oxygen atom [42–45].

Although strongly covalently bonded to the zeolite, hydrogen attached to the bridging oxygen atom reacts as a proton with reactant molecules and

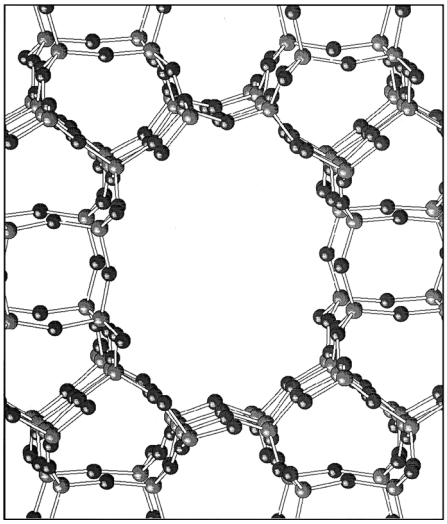

FIG. 2. The structure of mordenite zeolite.

hence induces transformation reactions known also from superacid catalysis [46–48]. However, as will be explained, the detailed mechanism of activation is very different from that known in superacid catalysis. Whereas in superacids low-temperature reactions generate carbonium and carbenium ions as stable but sometimes short-lived intermediates, the nature of carbonium

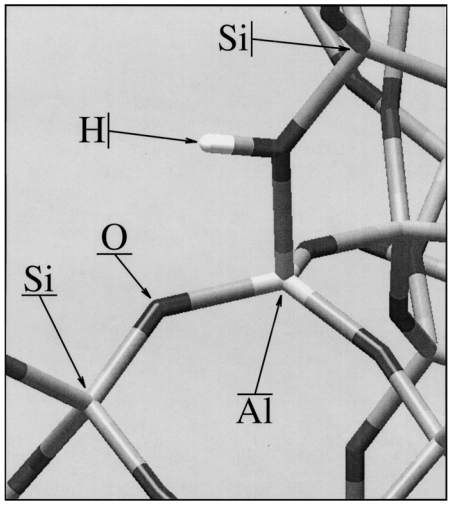

FIG. 3. Hydrogen bonded to a bridging O atom in mordenite.

and carbenium ion intermediates is often quite different in solid acid catalysis. Essentially, carbonium and carbenium cation intermediates are parts of transition states or activated intermediate states through which reactions proceed. The high activation barriers of the elementary reaction steps imply that zeolitic solid acids are weakly acidic compared to superacids. One way to understand this is that, different from superacid media, the dielectric constant of a zeolite is low ($\varepsilon \sim 4$) [49–51] and hence charge separation has a high energy cost [3].

It is now also well established that the zeolite framework has some flexibility. Due to the dominance of directed covalent bonding, the tetrahedra are rather rigid, but the bond-bending potential energy curve for bending of the Si–O–Si angle is rather flat. Local distortions of the framework can be easily accommodated because of the low energy cost of bending of the Si–O–Si angle. This is important because, as we will see later, attachment of a proton to the bridging oxygen atom increases the Si–O and Al–O distances and hence requires a larger volume than a free Si–O–Al unit. Upon deprotonation the Si–O and Al–O bonds decrease and hence the effective volume of the concerned tetrahedron decreases.

For low Al/Si ratio zeolites, differences in acidity of the zeolitic proton relate to slight differences in the local relaxability of the zeolite lattice around the protons [1–9]. For zeolites with a high Al/Si ratio, the zeolite proton interaction increases. Compositional variations may cause the deprotonation energy to vary by ~1–5%.

For a proper understanding of the interaction of hydrocarbons with zeolitic protons, it is important to realize that the oxygen atoms, with a computed charge close to -1, and the Si atoms, with a computed charge close to $+2$, have very different sizes. This is illustrated in Fig. 4. Oxygen atoms are relative large and the framework cations are small. This implies that hydrocarbon molecules, when adsorbed in the zeolite micropores, will experience mainly interactions with the large oxygen atoms, which inhibit direct interactions with the smaller lattice cations.

Bonding within the zeolite framework is mainly covalent, and ionic bonding contributes only ~10% [52–54]. The attractive interaction between the siliceous zeolite framework and hydrocarbons can best be described as a van der Waals dispersive interaction due to the attraction of fluctuating dipole moments of electronic motion on the oxygen atoms and hydrocarbons [55–59]. The van der Waals interaction

$$V_{\text{v·W}} = -\text{C}\frac{\alpha_i \alpha_j}{r_{ij}} \tag{3}$$

is proportional to the polarizabilities α_i of zeolitic oxygen atoms and, for instance, for alkanes the polarizabilities α_j of CH_2 or CH_3 units. The polarizability α_i is approximately proportional to the volume of a molecular unit.

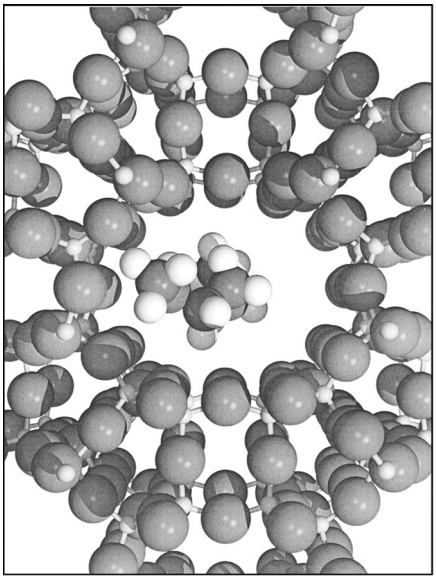

FIG. 4. Hexane occlude in a zeolite micropore.

In Eq. (3), C is a constant, and r_{ij} the distance between the centers of mass of units i and j [55–57]. Density functional theory quantum-chemical codes do not predict this van der Waals dispersive interaction accurately [60, 61].

One has to include the repulsive contribution to obtain the interaction potential. In the Lennard–Jones expression, the attractive and repulsive contributions can be described by

$$V_{\text{v·W}} = -4\varepsilon_{ij}\left(\left(\frac{\sigma_{ij}}{r_{ij}}\right)^6 - \left(\frac{\sigma_{ij}}{r_{ij}}\right)^{12} \right), \tag{4a}$$

where σ_{ij} is the sum of the van der Waals radius of i and j, and ε_{ij} the well depth [62]. However, the repulsive part of the potential is best described by the Born repulsion expression, leading to the Buckingham interaction potential:

$$V_{\text{v·W}} = -\text{C}\frac{\alpha_i \alpha_j}{r_{ij}^6} + Ae^{-ar_{ij}}. \tag{4b}$$

The Born repulsion expression stems from the Pauli principle, which results from the prohibition of electrons with the same spin occupying the same wavefunction, a situation that occurs when doubly occupied orbitals interact. Whereas the van der Waals interaction cannot be computed accurately from

DFT quantum-chemical codes, the Born repulsive interaction is accurately computed. Expressions (4a) and (4b) are two-body interaction potentials commonly used in codes that predict energies or geometries based on empirical potentials.

IV. Theoretical Approaches Applied to Zeolite Catalysis

We now report how theoretical methods can be used to provide information on the adsorption, diffusion, and reactivity of hydrocarbons within acidic zeolite catalysts. In Section A, dealing with adsorption, the physical chemistry of molecules adsorbed in zeolites is reviewed. Furthermore, in this section the results of hydrocarbon diffusion as these data are obtained from the use of the same theoretical methods are described. In Section B we summarize the capability of the quantum-chemical approaches. In this section, the contribution of the theoretical approaches to the understanding of physical chemistry of zeolite catalysis is reported. Finally, in Section C, using this information, we study the kinetics of a reaction catalyzed by acidic zeolite. This last section also illustrates the gaps that persist in the theoretical approaches to allow the investigation of a full catalytic cycle.

A. Simulation of Alkane Adsorption and Diffusion

1. Methods and Theory

Configurationally biased Monte Carlo techniques [63–65] have made it possible to compute adsorption isotherms for linear and branched hydrocarbons in the micropores of a siliceous zeolite framework. Apart from Monte Carlo techniques, docking techniques [69] have also been implemented in some available computer codes. Docking techniques are convenient techniques that determine, by simulated annealing and subsequent freezing techniques, local energy minima of adsorbed molecules based on Lennard–Jones- or Buckingham-type interaction potentials.

The interaction energy is determined by potentials as defined in Eq. (4). Bond-bending energy terms within the hydrocarbons are also included. The parameters of the interaction potential with zeolite have to be determined by a fit of experiment with theory. June *et al.* [66] and Smit and Maesen [67] used slightly different parameters (see Table I). The latter used parameters fitted on experimental adsorption isotherms of hexane in silicalite. Whereas in siliceous materials the dominant interaction term is given by the

TABLE I
VAN DER WAALS INTERACTION POTENTIALS FOR HYDROCARBONS ADSORBED IN ZEOLITES

Parameter set	$\sigma_{CH_3,O} = \sigma_{CH_2,O}$ (Å)	$\varepsilon_{CH_3,O}$ (K)	$\varepsilon_{CH_2,O}$ (K)
June *et al.* [66]	3.364	83.8	83.8
Smit and Maesen [67]	3.64	87.5	54.4

Buckingham potential, in zeolites with protons or cations additional interaction terms become important. We discuss the interactions with protons later, but here we comment briefly on the effect of the presence of cations in zeolite micropores. Kiselev and Quang Du [68] were among the first to analyze adsorption in the hydrocarbon–zeolite system. Cations other than protons have a charge close to their formal valency. Therefore their bond with the negative charge of the framework is predominantly of an ionic nature. These cations will generate large electrostatic fields. The interactions with apolar hydrocarbons can best be described by the inductive interaction of a polarizable particle i defined by its polarizability α_i and an ion j with charge q_j:

$$V_{\text{ind}} = -q_j^2 \frac{\alpha_i}{2r_{ij}^4}, \tag{5}$$

where r_{ij} is the distance between particle i and particle j [55–57, 68]. Kiselev and co-workers provided empirical potentials that can be used for adsorption in ion-exchanged zeolites.

The equilibrium Monte Carlo method computes thermodynamic averages by simulating equilibrium configurations. Hence it is an adequate technique to compute free energies. In essence, four steps are used.

- Give the adsorbate a random new position and random new configuration.
- Calculate the energy difference between this new configuration and the old configuration.
- Accept this new configuration with a probability P proportional to Boltzman's weight factor at temperature T:

$$P \cong \exp\left(-\frac{E_i}{kT}\right).$$

- Repeat; this generates a chain of configurations Γ_i.

The thermodynamic average is then computed from

$$\langle A \rangle = \frac{1}{m} \sum_i^m A(\Gamma_i), \tag{6}$$

where i sums up the number of configurations.

2. Simulation of Alkane Adsorption Isotherms

One of the most fascinating results of these simulations is the strong dependence of the cavity site on the size and shape of the adsorbing molecule and cavity. For instance, for the zeolite ferrierite, theory and experiment show that whereas propane preferentially adsorbs in the 8-oxygen atom ring pockets, pentane and the longer hydrocarbons preferentially adsorb in the one-dimensional 10-ring channel system [70, 71]. Only at higher occupations do some of the molecules become forced into the eight-ring pocket. In addition, at higher coverages orientational packing of molecules may occur, again dependent on the match of the molecule length and the free micropore length, giving rise to plateaux in the adsorption isotherm [72, 73].

Figure 5 illustrates the dependence of the energy of adsorption for linear alkanes of increasing chain length for different zeolites. An optimum in the

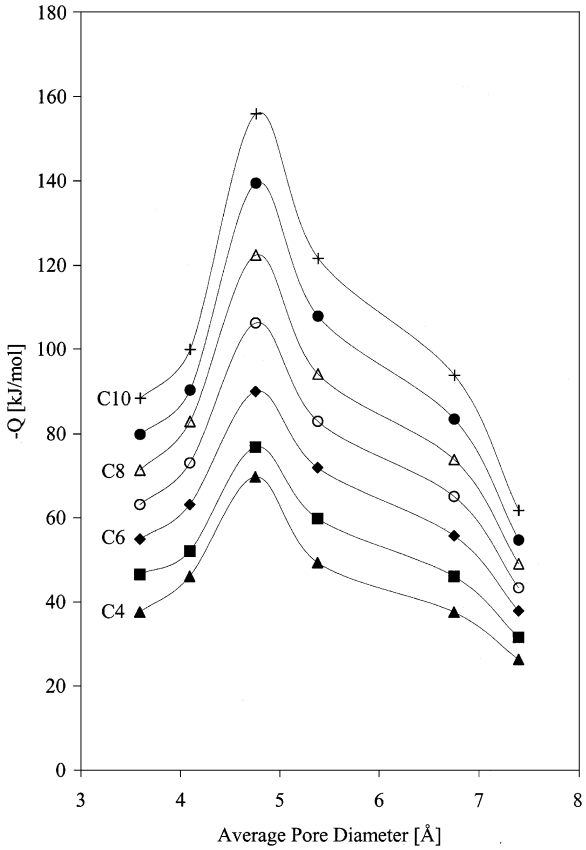

FIG. 5. Computed enthalpies of adsorption of linear hydrocarbons as a function of the average zeolite micropore diameter [70].

adsorption energy is found as a function of the average micropore diameter. Also, an incremental increase in the energy of adsorption with increasing chain length is observed. The basic feature that Fig. 5 illustrates is that the energy of adsorption increases with decreasing microchannel dimension. The optimum arises since there is no access of micropore or cavity when their size is too small. To the left of the optimum, zeolites have a bimodal micropore distribution of very narrow inaccessible pores and wider pores with low interaction energies. The increase in energy of adsorption with decreasing micropore channel is due to the increasing attractive van der Waals interaction with decreasing distance of the alkane CH_2 and CH_3 groups with micropore oxygen atoms.

Table II [74] shows a comparison of computed and measured energies of adsorption for two hydrocarbons and two zeolites. Whereas mordenite (MOR) has a one-dimensional 12-ring channel system, ZSM-22 (TON) has a one-dimensional 10-ring channel system. One notes again the increase in energy of adsorption with decreasing channel dimension. There is also good agreement with experiment, except for zeolites that contain a substantial concentration of protons. In this case there is an increase in energy by 8–15 kJ/mol. Interestingly at $T = 513$ K, a typical reaction temperature, the equilibrium constants of adsorption K_{ads} are smaller for the narrow-micropore zeolite TON than the wider-micropore zeolite MOR. The larger loss in mobility due to the larger confinement in the smaller pore causes a larger loss of entropy and hence counteracts the gain in the energy of adsorption in the smaller micropore. As a consequence, at this temperature the micropore occupation of the medium-sized MOR pore by hydrocarbons is

TABLE II
MEASURED AND SIMULATED HEATS OF ADSORPTION AS WELL AS HENRY ADSORPTION COEFFICIENTS FOR LINEAR HYDROCARBONS IN SILICEOUS ZEOLITES

	$-\Delta H_{ads}$ (kJ/mol)		K_{ads} ($T = 513$ K) (mmol/gPa)	
	Simulation [74]	Literature	Simulation [74]	Literature
n-Pentane/TON	63.6	71 [75]	$4.8 \cdot 10^{-6}$	$4.6 \cdot 10^{-6}$ [75]
		62.1 [76]		$6.53 \cdot 10^{-6}$ [76]
n-Pentane/MOR	61.5	59 [75]	$4.8 \cdot 10^{-5}$	$6.8 \cdot 10^{-5}$ [75]
		55.7 [76]		$8.6 \cdot 10^{-5}$ [76]
n-Hexane/TON	76.3	82 [75]	$1.25 \cdot 10^{-5}$	$8.0 \cdot 10^{-6}$ [75]
		75.0 [76]		$1.99 \cdot 10^{-5}$ [76]
		72.3 [77]		$7.8 \cdot 10^{-6}$ [77]
n-Hexane/MOR	69.5	69 [75]	$1.26 \cdot 10^{-4}$	$1.9 \cdot 10^{-4}$ [75]
		67.1 [76]		$5.5 \cdot 10^{-4}$ [76]
		69 [77]		$1.3 \cdot 10^{-4}$ [77]

substantially higher than that of the smaller-pore zeolite TON. The general consequence of these results is that an optimum zeolite micropore size provides for a maximum pore occupation. When the pore size is too large (e.g., faujasite or a clay surface), the low energy of adsorption gives a low micropore occupation. On the other hand, when the accessible pore size becomes too small, again, a low micropore coverage results because of the increasing loss of entropy.

For the overall rate of a catalytic reaction, this is an important conclusion because the rate of a catalytic reaction is proportional to the site occupancy and the rate constant of molecular activation, when the latter step is rate limiting. For a monomolecular reaction this follows from an elementary expression for the overall rate r:

$$r = V\frac{d[P]}{dt} = k_i \cdot \theta, \tag{7}$$

where k_i is the elementary rate constant of activation of the adsorbed molecule and θ is the coverage by reactant molecules on catalytically active sites. $[P]$ is the concentration of product molecules and V the volume. We discuss in the next section the computation of k_i using quantum-chemical methods. Equation (7) illustrates the proportionality of rate with micropore filling. It can also be used to illustrate that even when k_i does not depend strongly on micropore size (which is often the case), the overall rate may depend strongly on the micropore size. This follows from the micropore size dependence of θ. In the case that θ can be described by Langmuir adsorption and the competitive product or intermediate adsorption is ignored, expression (7) can be rewritten

$$r = k_i \cdot \frac{K_{\text{ads}} \cdot [R]}{1 + K_{\text{ads}} \cdot [R]} \tag{8}$$

where $[R]$ is the concentration in reactant. From (8), one finds the following expression for the apparent activation energy of the rate r:

$$E_{\text{app}} = E^i_{\text{act}} + (1 - \theta)E_{\text{ads}}, \tag{9}$$

where E^i_{act} is the activation energy of the intrinsic rate constant k_i, and E_{ads} the energy of adsorption. Usually, E^i_{act} is only weakly dependent on the micropore size. However, Eq. (9) implies an important dependence of the rate of the overall reaction as a function of the micropore size and shape because of their strong relation to E_{ads}.

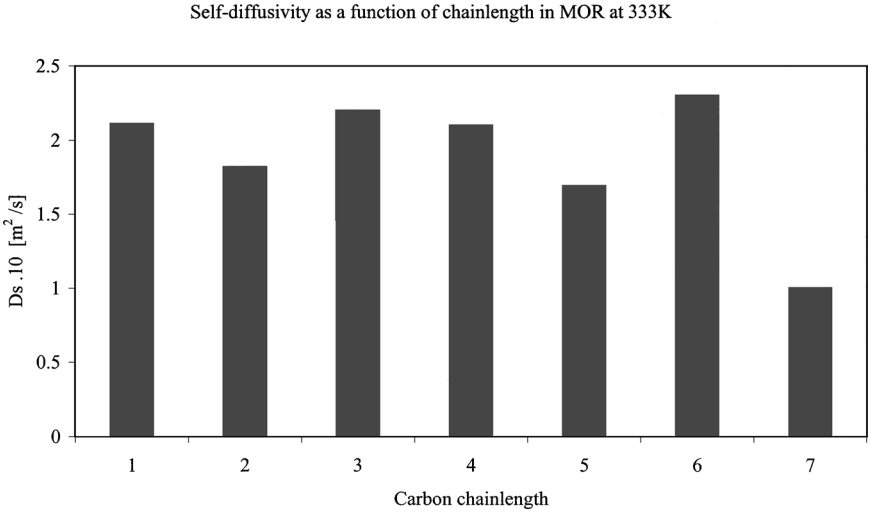

FIG. 6. Simulated self-diffusivity diffusion constant as a function of linear hydrocarbon chain length in mordenite [78].

3. Simulation of Diffusion

Rates of diffusion of linear and branched alkanes by zeolites within medium-sized pores are very fast. This is illustrated for linear alkanes in Figs. 6 and 7. As shown in Fig. 6, the self-diffusion constant in mordenite that has one-dimensional micropores is fast and independent of the length of hydrocarbons [78]. On the other hand, for the wider-pore zeolite faujasite, there is a decrease with chain length. This illustrates that in the cavities of mordenite, diffusion is controlled by the interaction with the zeolite wall. Diffusion within mordenite can be characterized as a creeping motion. In the larger micropores of faujasite, diffusion is more liquid-like [79]. Figure 7 [78] shows a higher initial diffusion rate for the zeolite with a larger micropore. Very similar and still fast rates of self-diffusion are found when the micropores become half-filled.

The diffusion constants are computed by solving Newton's equation of motion, maintaining the average kinetic energy equal to $3/2\ kT$. Whereas generally there is no need to include explicitly the fluctuating motion of lattice atoms, this is critical when diffusion causes molecules to move through windows of size comparable to the lateral dimension of these molecules [85–88]. The activation energies for self-diffusion may differ widely. For highly branched molecules or alkyl-substituted aromatic molecules, it may severely inhibit actual mobility at reaction temperatures [89]. Under such conditions not only conversion may become diffusion limited, but also

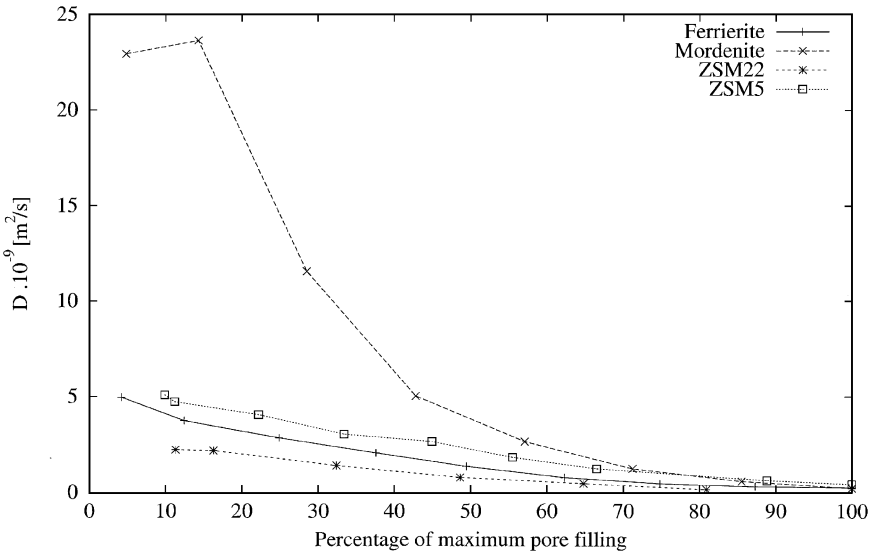

FIG. 7. Simulated *n*-butane self-diffusivity constant as a function of micropore filling at 333 K [78].

selectivity. For instance, alkylation of toluene into the *p*-xylene catalyzed by ZSM-5 is highly selective when the rate becomes diffusion limited [90]. Then only *p*-xylene has a diffusional rate high enough to move out of the zeolite crystallites. To compute the yield of a reaction in such a case, coupling of the reaction rate and diffusion will have to be explicitly considered. We refer to the work of Hinderen and Keil [91], who introduced kinetic Monte Carlo techniques to predict zeolite kinetics. In the next section we discuss the kinetics of zeolite-catalyzed reactions for which self-diffusion is not rate limiting.

A general experimental result is the difference between measured rates of diffusion in macroscopic experiments and measurements of self-diffusion by spectroscopic techniques such as gradient field NMR [80–84]. The difference between the microscopic measurement and the macroscopic experiment is desorption and reentry of molecules in zeolite microcrystallites. In this respect, it is important to remember the Biot condition, which states the condition when the measured rate of diffusion is independent of the rate of desorption:

$$k_{\text{des}} \gg \frac{D}{R^2}. \tag{10}$$

It shows that when the size of a particle is large enough the time scale of diffusion becomes long compared to the time scale of desorption. When

the rate of desorption interferes a strong dependence of the overall rate of diffusion on the particle size should be measured.

B. Hydrocarbon Activation by Zeolitic Protons

The great contribution of quantum chemistry has been the proper understanding of the nature and energetics of carbonium and carbenium ion intermediates, as they occur in zeolites. Carbonium ions, organic cations in which one or more carbon atoms become five coordinated due to proton attachment, and carbenium ions, organic cations in which a carbon atom is three coordinated and has become planar, have been observed as short-lived species using NMR spectroscopy in superacids [92, 93]. Because of the similarity of the type of reactions that are catalyzed, it has been thought that zeolites have a similar superacidity. However, there is now ample experimental and theoretical evidence showing that this is in fact not the case. We summarize the theoretical evidence here.

The elementary reaction steps of the hydrocarbons considered in this section are summarized in Fig. 8. The occurrence of monomolecular reactions with linear hydrocarbons that produce hydrogen and alkane fragments was first demonstrated by Haag and Dessau [94]. For convenience, the zeolite lattice to which the proton is attached is not explicitly shown in the scheme. However, it will become clear later that proton activation cannot be understood properly without explicitly taking into account the interaction of the carbonium and carbenium ion intermediates with the negatively charged zeolite wall.

Russian scientists concluded at the end of the seventies that proton activation and formation of organic cations could occur only when the positively charged protonated intermediates become stabilized by the negative charge left on the zeolite lattice [95–100]. Ten years later quantum-chemical calculations confirmed this conjecture. The finding was that these organic cations cannot exist as stable intermediates unless sterically constrained [101]. They are typically part of transition states. This is illustrated in Figs. 9a and b [102]. For carbenium ion intermediates from alkenes, this was first shown in an ab initio calculation by Kazansky and Senchenya [103] and Kramer *et al.* [104] for carbonium ion intermediates. Physically, this arises from the high energy cost of splitting the OH bond heterolytically. The corresponding energy cost is ~1250 kJ/mol. Fortunately, when a molecule is protonated or, in other words, activated by a proton, no full cleavage of the OH bond is necessary. Typical activation energies are of the order of 10% of the full OH bond cleavage energy. The energy cost of bond cleavage is compensated for by the proton attachment energy (~200 kJ/mol) and electrostatic

A. Direct activation processes:

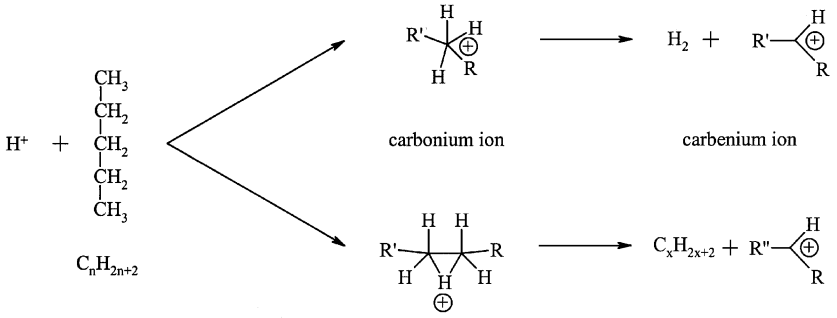

B. Carbonium mediated processes are circumvented by:

1. Chain processes mediated via *hydride*-transfer:

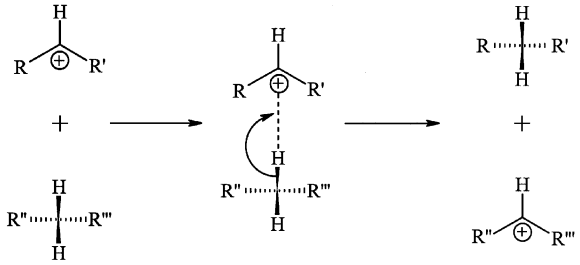

2. Noble metal promoted bifunctional catalysis establishes equilibrium:

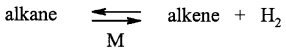

C. Protonation of alkene generates carbenium ions:

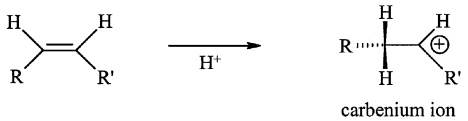

FIG. 8. Initial elementary reaction steps of linear alkanes.

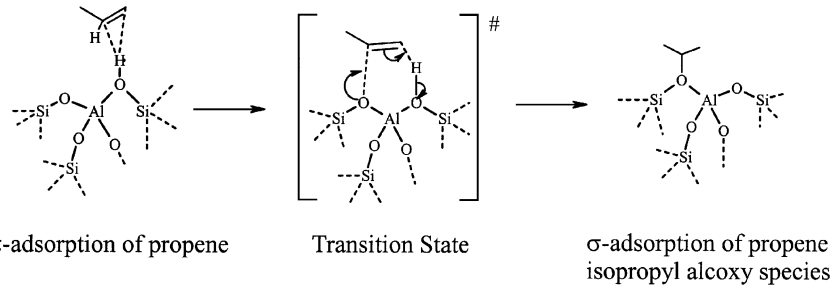

FIG. 9a. Schematic representation of the geometries of propene during its protonation attack mechanism by chabazite.

stabilization (∼900 kJ/mol) with the negative charge that develops on the zeolite framework when the proton is transferred. The major difference between superacids and zeolites is that in superacids cations and anions become solvated by the polar solvent molecules. No such stabilization occurs in zeolites. The chemistry in zeolites, when applied in hydrocarbon catalysis, is much closer to that in a vacuum (dielectric constant $\varepsilon \sim 4$) than to that in a polar medium such as a polar superacid (dielectric constant $\varepsilon \sim 80$–100).

Until quite recently, quantum-chemical calculations on proton activation by zeolites were possible only using the cluster approximation [13–31]. A representative cluster is shown in Fig. 10 [105]. It initially seems surprising that calculations based on such small clusters can actually predict a property of a periodical system suchas a zeolite. Two basic features of bonding in the zeolitic framework are relevant in this respect. First, chemical bonding is largely covalent: 90% of bonding can be described as due to covalent interaction, and only 10% of the bond strength is due to electrostatic interaction ions. Second, the flexible nature of the zeolite lattice can readily accommodate deformations due to the presence of the proton at a relatively low energy cost. Key to the use of the cluster approximation is termination of the cluster by hydride, a hydroxyl ion, so as to make the cluster neutral [1–8, 17]. The activation energies of protons in reactions with hydrocarbons can be computed with an accuracy of ∼30 kJ/mol, using programs based on DFT [106–108]. Such quantum-chemical calculations scale much more favorably with the number of electrons in a system ($n^{2.6}$) than Hartree–Fock-based codes ($n^{4.2}$ for the MP2 method).

Due to the covalent nature of chemical bonding, properties of zeolitic protons depend on local electronic structure details. This is illustrated in Fig. 10 [105]. Using a basis set that predicts the NMR quadrupole coupling constants (QCC), accurately measured QCCs in zeolite ZMS-5 for Al tetrahedra in the proton form and deprotonated Al tetrahedra (e.g., by cation exchange) are compared with predicted QCCs from cluster model calculations. One

FIG. 9b. Geometries of propene during its protonation attack mechanism by chabazite as obtained from DFT periodical structure optimization calculations. Details of the propene geometry (values in degrees) are shown. The geometry of propene when the transition state occurs is very similar to the geometry of an isopropyl carbenium [102].

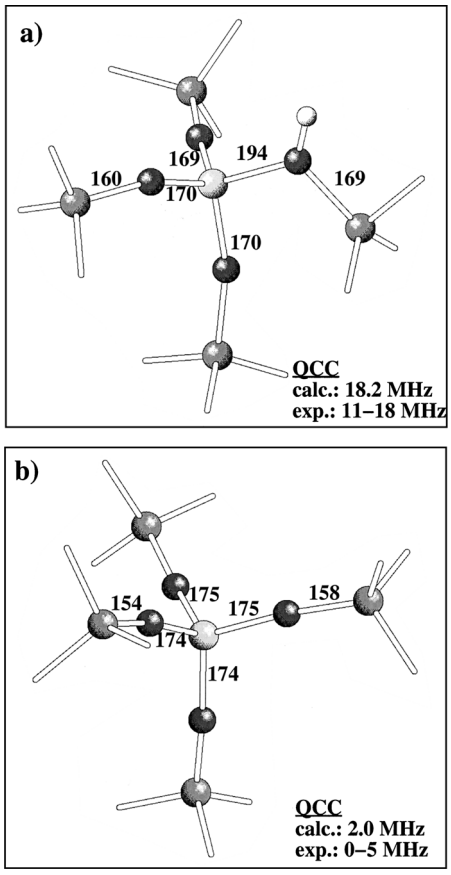

FIG. 10. The geometries of zeolitic site clusters for a protonated cluster (a) and a deprotonated cluster (b) (bond lengths in pm). The values are the quadrupole interaction parameters computed from the cluster models compared with experimental data [105].

notes the agreement between theory and experiment. Such agreement is typical also for other physical properties of the proton and its charge as reflected in the proton chemical shift [109, 110] or vibrational frequency [111, 112]. Note the asymmetric distortions of the protonated cluster in Fig. 10. The computed Al–O bond length of the cluster in its global energy minimum lengthens when a proton becomes attached to the bridging oxygen, which is a behavior indicative of covalent bonding. These results also illustrate the importance of geometry optimization of the computational systems. Only when this is done properly do computed interactions start to converge with experiment. When the protonic site is part of the

TABLE III
CALCULATED ACTIVATION ENERGIES ($E^{\#}$) FOR SOME ELEMENTARY REACTION STEPS OF ISOBUTANE COMPARED WITH EXPERIMENTAL NUMBERS EXTRACTED FROM KINETIC DATA [17, 113]

Reaction	Calculated $E^{\#}$ (kJ/mol)	Experimental range (kJ/mol)
Protolytic cracking	50.4	43–53
Protolytic dehydrogenation	60.6	40–50
Hybride transfer	36.0	<40–53
To *s*-C_3	41.0	
To *t*-C_3		

zeolite lattice, clearly the large distortions of the cluster when reaction with proton transfer occurs have to be accommodated by lattice relaxation for the cluster approximation to be used at all. As discussed before this can occur with very little expense of lattice energy. A major zeolite property that cannot be studied with this very small cluster is the effect of steric matching of the zeolite micropore and the size of the transition state complex. Using periodical calculations based on plane waves, this now becomes directly accessible to calculation, as we discuss later. We analyze transition-state geometry and energy results in clusters first and return to the size issue later.

Table III gives a comparison between computed and experimental activation energies for elementary proton-activated reaction steps of isobutane computed on a small cluster [17, 113]. We recognize the three reactions shown in Fig. 8. The first two reactions are monomolecular reaction steps. The bimolecular hydride transfer reaction is an elementary reaction step that maintains the catalytic reaction cycle: without a carbonium ion an intermediate transition-state formation occurs. As also shown in Fig. 8, an "intermediate" carbenium species (which actually exists as an alkoxy intermediate) can react in two ways to yield a product molecule. Hydride transfer from a reactant molecule produces an alkane, and proton backdonation produces an olefin. In the latter case, the reaction cycle can be continued only when a reactant molecule becomes activated by direct reaction with the proton. As explained before, the relatively high values for the activation energies stem from strong covalent bonding of the zeolite O–H and zeolite O–C bonds of intermediate alkoxy species. The high energy cost is due to the need to stretch these bonds to reach a transition state in which the carbenium ion is more or less free to react. One way of formulating this is that in zeolites reactions occur on top of the potential energy hills, instead of close to the energy valleys as for solvated species.

As has been shown, especially by Zygmunt *et al.* [114] but also by others [113, 115], computed activation energies depend substantially on the size and connectivity of the zeolite model clusters. In general, slow convergence is obtained for the deprotonation energies as a function of cluster size. There is an elegant procedure to obtain rapid convergence [17]. The activation energy (E_{act}) depends on the difference in energy of the cationic transition state (E_{cat}) with a very weak covalent but strong electrostatic interaction and the deprotonation energy in which a strongly covalent bond is broken:

$$E_{\text{act}} = E_{\text{cat}} - E_{\text{deprotonation}}. \tag{11}$$

One expects E_{act} to vary as a function of the cluster size mainly because of variations in the deprotonation energy. Hence a plot of E_{act} versus $E_{\text{deprotonation}}$ should result in a straight line (see Fig. 11). For each deprotonation energy the line gives the predicted value of the activation energy. Spectroscopic measurements of spectral shifts by adsorption of weakly interacting basic molecules allow the determination of deprotonation energies for a proton [117–119]. One notes in Table III the general agreement between computed and experimentally determined activation energies. Whereas the orders of magnitudes are correct, one also notes, however, that values tend to be overestimated by 30 or 40 kJ/mol.

Recently, studies have been made on related transition states but in periodical structure calculations [120–122]. The results for cluster and periodical calculations have been compared: significant reductions of the energy have been found for transition-state energies. Also, calculations from large cluster models that contain cavities have led to the same results [50, 111]. Whereas the energies of transition states appear to be influenced strongly by the zeolite topology, this is much less the case for the initial or final steps in the protonation reaction. Very differently from the dominantly covalent bond of the ground-state OH or alkoxy groups, the structures that correspond to transition states are highly polar. Positive charge is distributed over the cationic part of the molecule and negative charge is localized around the Al-containing lattice tetrahedral site. The transition-state complex creates a large dipole in the cavity. The high polarizability of the oxygen atom cavity stabilizes this complex by a screening interaction, E_{scr},

$$E_{\text{scr}} \approx -\frac{1}{2}\alpha_{\text{c}} E_{\Gamma}^2 = -\frac{1}{2}\alpha_{\text{c}} \frac{\mu^2}{R^4}, \tag{12}$$

where α_{c} is the polarizability of the cavity, $\vec{E}_{\Gamma}$ the electrostatic field from the transition-state dipole ($\vec{\mu}$), and R the approximate radius of the cavity. Of course this stabilization is expected to be larger for a small cavity than a larger one. Stabilization energies as high as 50–70 kJ/mol have been reported

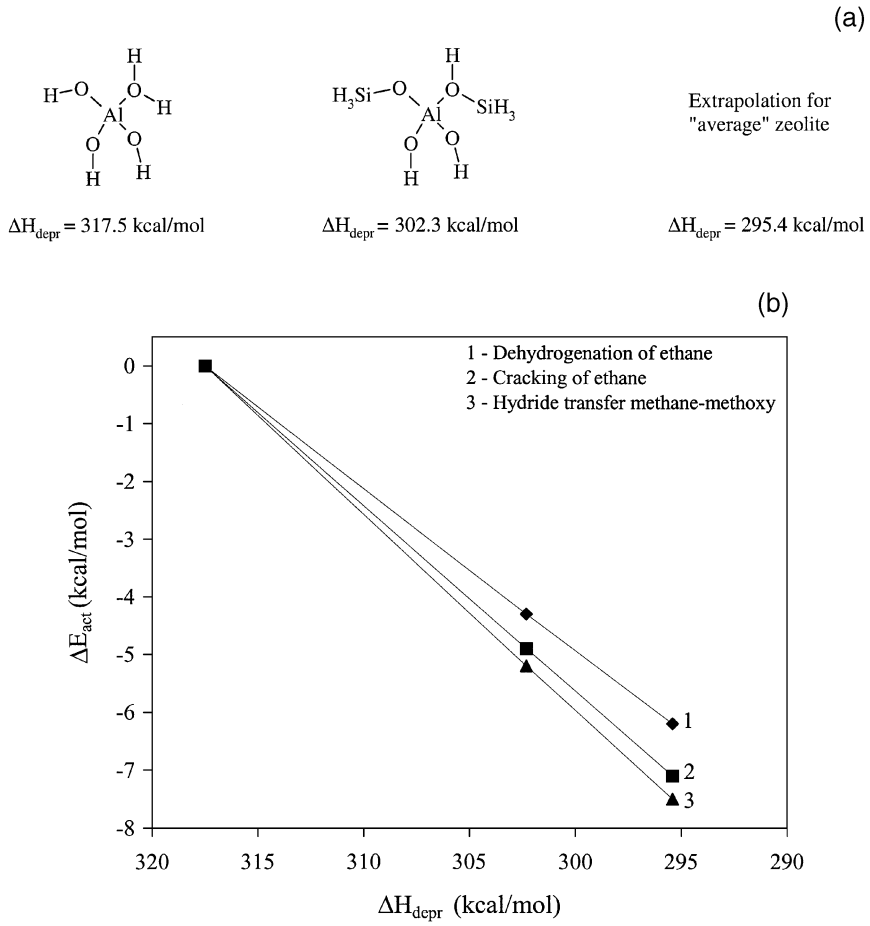

FIG. 11. Corrections to the calculated activation energies for the cluster acid strength. Activation energies for protolytic cracking of ethane, protolytic dehydrogentation of ethane, methane–methoxy hybrid transfer, and methane deprotonation energies are computed at the MP2/6-31++G**//HF/6-31G* level with the ZPE corrections [17, 113].

[43, 123]. The van der Waals interaction between cavity and hydrocarbon is expected not to change significantly between the ground and the transition state, because the size of the hydrocarbon part does not change. A comparison of cluster-computed and periodical DFT-computed chemisorption of propylene is shown in Table IV.

Before continuing the analysis of pore size dependence, a remark must be made on the comparison between theoretical and measured data as done

TABLE IV
DFT COMPUTED VALUES OF THE CHEMISORPTION REACTION OF PROPYLENE ON AN ACIDIC ZEOLITE CATALYST[a]

Energy comparison	Cluster approach (kJ/mol)	Periodical approach (kJ/mol)
E_π	−23	−27
E_{act}	105	47
E_σ	−52	−61

[a]The DFT energies of the reaction on a 4T zeolite cluster are compared with the periodical electronic structure results for chabazite. The computed energies are the π-complex energies with respect to the gas-phase system (E_π), the activation energies with respect to the π-complex (E_{act}), and the energies of σ-complex (E_σ) with respect to the gas phase [122].

in Table III. The experimental kinetic parameters were obtained from a kinetic analysis in which overall experimental data were deconvoluted so as to obtain elementary rate constants. In the next section, we show how this can be done. A prerequisite is knowledge of the reaction mechanism. The reaction mechanism used to deconvolute the experimental data used in Table III has been chosen as consistent with that as theoretically proposed and discussed in this paper.

Apart from the use of periodical or very large cluster quantum-chemical calculations, embedding techniques can be applied to analyze consequences of steric constraints. These embedding methods are quantum mechanics/molecular mechanics-related techniques [11, 50, 112, 123– 128]. The quantum-chemical cluster is embedded in a lattice described by classical interactions, such as electrostatic, van der Waals, or repulsive interactions. Care has to be taken to compensate for boundary effects between the quantum-mechanical neutral cluster, terminated with hydride or hydroxyl groups, and the lattice atoms. The lattice atoms and cluster atoms can be imagined as being connected by bonds that give relaxation constraints to the cluster. Sauer and co-workers [11, 50, 112] have developed an embedding approach that enables embedded calculation of ground states and transition states, but separate development of potentials for both states using quantum-mechanical cluster calculations to provide potential energy surfaces is necessary.

An alternative method is the Chem-Shell embedding procedure developed by Greatbanks *et al.* [124]. This method does not require the development of new force fields as a function of intermediate states [123–128]. Using the Chem-Shell procedure, an interesting result has been obtained for the protonation of isobutene in chabazite. The results are illustrated in Fig. 12 [123]. The quantum-mechanical calculations were done within the

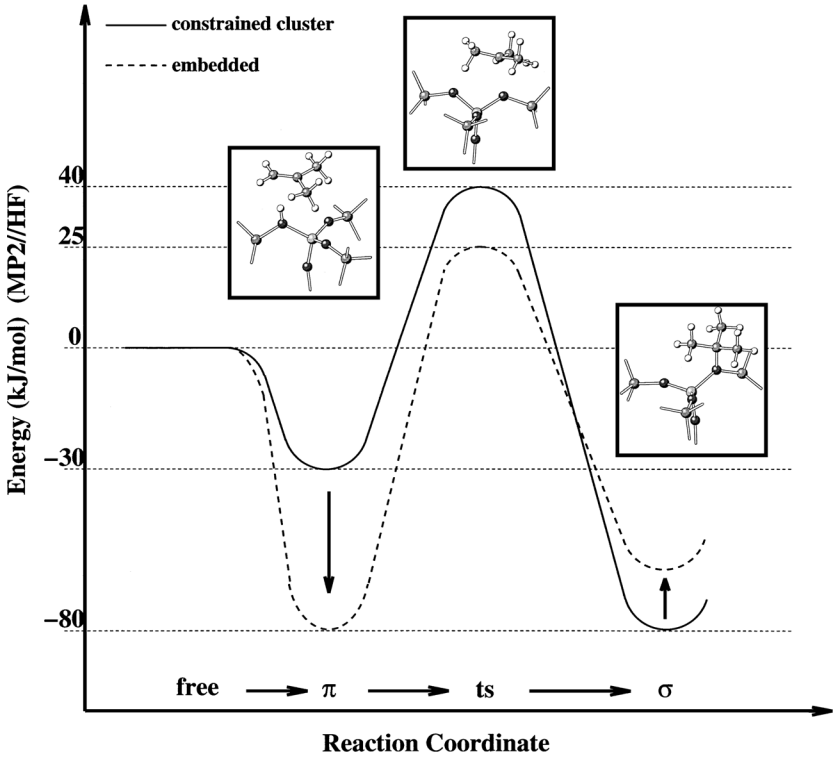

FIG. 12. Effect of embedded environment on the stability of *i*-butene activation at a Brønsted-acid site in chabazite [123].

Hartree–Fock approximation. The interaction of the π bond with a proton leads to different states: the first one is a weakly π-bonded state for which the interaction energy between the proton and the olefin π bond is about 30 kJ/mol, and the second one is a σ-bonded state or alkoxy species in which protonation and chemisorption of isobutene have occurred. The protonation of isobutene gives a $C^+(CH_3)_3$ carbenium ion that binds to a lattice oxygen atom that bridges lattice Al and Si. In the transition state from the π-state to the σ-state, protonation and chemisorption are associated. The curves drawn in Fig. 12 present the relative energies of the π-bonded state, σ-bonded state, and transition state between these two states. One notes the strong stabilization of the σ-bonded protonated state compared to the weakly bonded π-state. Interestingly, the relative energies of the π- and σ-bonded state change completely for the embedded situation. Compared to the π-bonded state, the σ-bonded alkoxy state now appears to be destabilized. This is because of steric repulsive interactions that arise when the alkoxy O–C bond

brings the methyl groups of isobutyl close to oxygen atoms in lattice tetrahedra neighboring the Al-containing tetrahedron. The strong repulsive interactions that arise prevent the formation of a strong O–C alkoxy bond. Alkoxy formation is actually prevented and the promoted intermediate is now close to a free carbenium ion, a result recently confirmed by full DFT periodical electronic structure calculations of SAPO-5 [129], which has cavities similar to those of chabazite. For the hydrogen-bonded π-state with a larger O–C distance, a more favorable interaction than the free cluster is found. This is due to the additional stabilizing interaction of the isobutene molecule now possible with the other oxygen atoms from the chabazite cage. The extra stabilization is here due mainly to the attractive van der Waals interaction. These results illustrate the importance of including the attractive van der Waals interaction as well as Born repulsion effects for bulky molecules and intermediates in estimates of protonation of molecules. Both contributions are strongly micropore size and shape dependent. The protonation of the olefin now leads to a state close to a carbenium ion.

We now introduce the two ways in which these pore size-dependent terms can be added as corrections to cluster calculations on small clusters not containing any information on the micropore as shown in Fig. 10. It is important to remember that the attractive van der Waals interaction cannot be properly calculated with currently used quantum-chemical DFT methods. How to correct for the attractive part is illustrated in Fig. 13. The figure illustrates that the protonation energies with respect to the gas phase have to be considered as the summation of two energetic interactions:

$$\Delta E_{\text{sys}} = \Delta E_{\text{ads}} + \Delta E_{\text{sys}}(\text{local}), \tag{13}$$

where ΔE_{ads} is the energy of adsorption of the molecule in the siliceous part of the zeolite. This is the strongly micropore size- and shape-dependent adsorption energy discussed in Section IV. ΔE_{sys} (local) is the quantum-chemical enrgy of the considered system (i.e., π-state, transition state, or σ-state) with respect to its noninteracting state (or gas-phase state). Expression (13) is based on the approximation that in the different states the van der Waals interaction energy does not change, since protonation concerns only a small part of the molecule [130]. The implication of expression (13) is that differences in protonation energies of different zeolites are due mainly to differences in the ΔE_{ads} term of the expression. However, one should not assume that corrected protonation or activation energies obtained from calculations simply reflect the differences in chemical reactivity of the zeolitic proton. Experimentally, the zeolite deprotonation energy of differently located protons varies between 10 and 30 kJ/mol for a zeolite with a Si/Al ratio below 10. Embedded calculations or periodical calculations can be used to estimate this quantum-chemical protonation energy as a function of

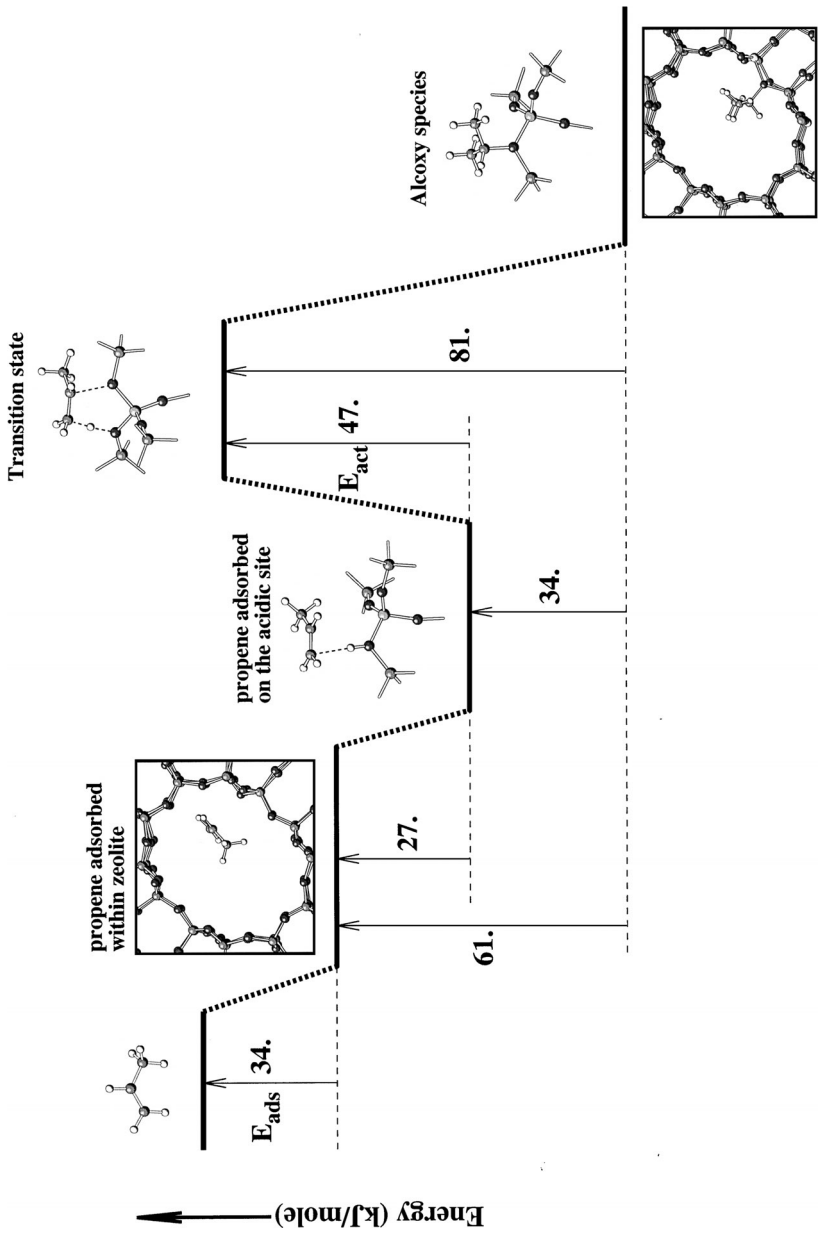

FIG. 13. Changes in energy of adsorption of a protonated molecule with respect to the gas phase for protonation of propylene in chabazite. E_{ads} is the adsorption energy of propene in chabazite.

the proton position in a zeolite. As we will see the additivity concept basic to expression (13) is important in understanding catalytic acidity. It is important to decouple the cavity size-dependent van der Waals contribution, which relates to adsorption, from the chemical reactivity, which relates to the interaction with the proton. The repulsive interactions of bulky molecules with the zeolite micropore are very important for selectivity differences of conversion reactions controlled by steric constraints.

Embedded or periodical calculations are essential to compute these effects properly. A recent study of alkylation of toluene using a DFT periodical electronic structure code demonstrated the feasibility of this approach [131]. We illustrate here how Eq. (13) can be used to compute corrections to the activation energy from the cluster approach by adding the repulsive interaction that results from the formation of bulky intermediates. We use as an example the bimolecular hydride transfer reaction. The activation energy of the corresponding elementary rate constant can then be written

$$\Delta E_{\text{act}} = \Delta E_{\text{act}}(\text{cluster}) + \Delta E_{\text{steric}}, \tag{14}$$

where ΔE_{steric} is the repulsive term in the activation energy, which depends strongly on the micropore volume and shape.

Transition states of the hydride transfer reaction have been studied quantum chemically using the cluster approach [132, 133]. In the transition state, the hydrogen atom becomes positioned between the two carbon atoms, in between which the hydrogen atom changes its position. In Fig. 14, the schematic

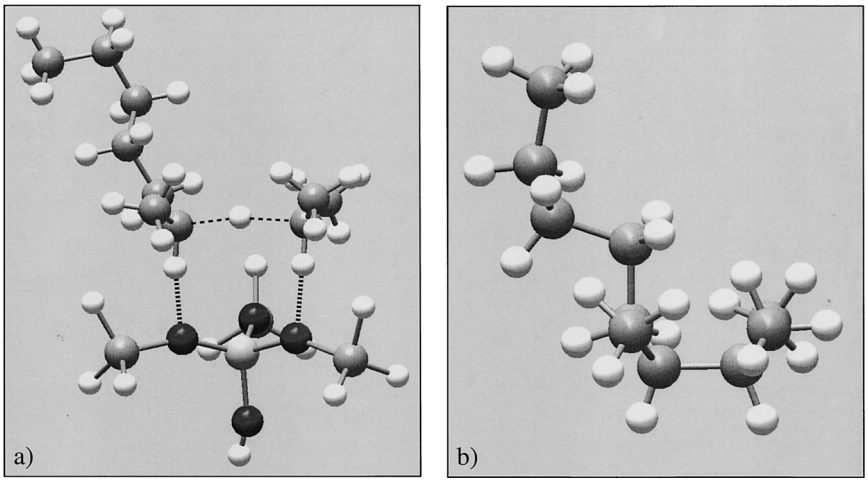

FIG. 14. (a) Schematic geometry of the transition state for hydrogen transfer between heptane and propyl alkoxy. (b) Schematic geometry of the 2-propyl-2 heptane isomer of decane [17].

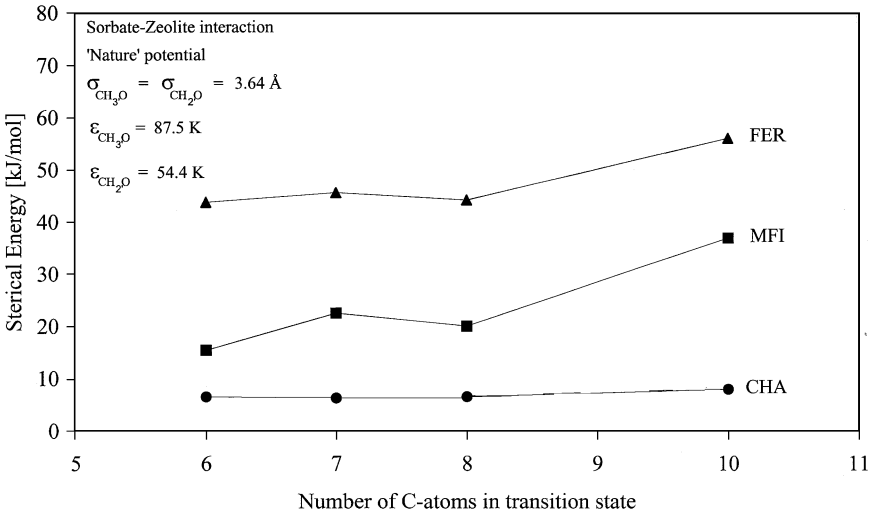

FIG. 15. Energy contribution to the transition-state energy due to sterical effects for hydride transfer reactions in three zeolites [74].

transition state for hydride transfer between heptane and propyl is sketched. As can be noted from Fig. 14b its structure is close to that of the 2-propyl-2-heptane isomer of decane.

Figure 15 gives the computed differences in energy according to a Monte Carlo simulation for a few zeolites [74]:

$$\Delta E_{\text{steric}} = E_{\text{ads}}\,(\text{intermediate}) - E_{\text{ads}}\,(\text{reactant}\,1) - E_{\text{ads}}\,(\text{reactant}\,2). \quad (15)$$

One notes the strong dependence of ΔE_{steric} as a function of the type of zeolite and also the large repulsive correction ΔE_{steric} for the zeolite with the narrow one-dimensional pore (ferrierite). We illustrate in the next section how the values of ΔE_{steric} can be used to assist kinetic analysis.

C. KINETICS

The aim of this section is to illustrate how the mechanistic principles as well as the rate constant predictions outlined in the previous section can be used to simulate the overall rate of a reaction. It also provides an opportunity to discuss more extensively the meaning of relation (13). This is done using experimental data on the hydroisomerization of hexane.

The hydroisomerization reaction occurs in an excess of hydrogen (H_2/hexane ~ 30) catalyzed by noble metal (e.g., Pt)-activated acidic zeolites. The mechanism of the reaction is rather well understood and the sequence of

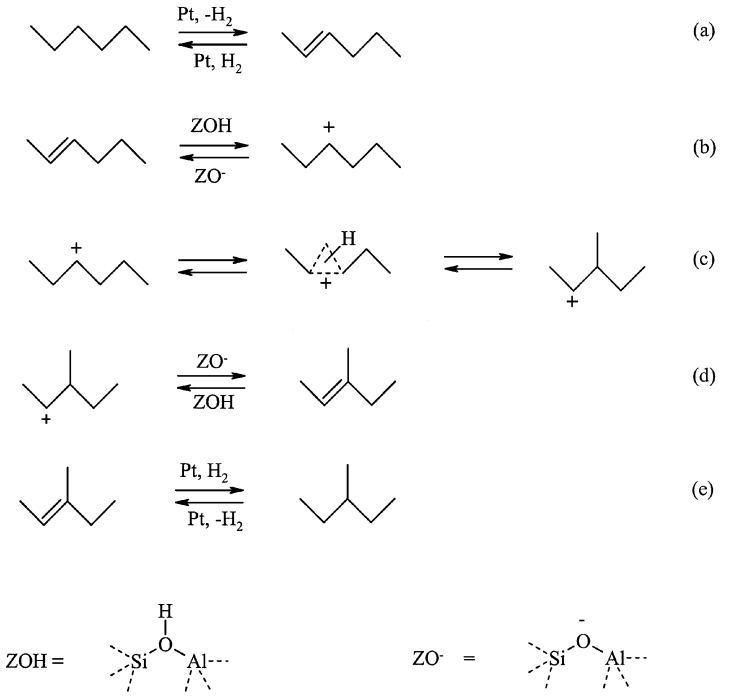

FIG. 16. Reactions involved in the hydroisomerization reaction: (a) equilibration of *n*-hexane and *i*-hexane (leading experimentally to a [hexane]/[hexene] ratio of approximately 10^{-6}), (b) protonation of hexene, (c) isomerization of *n*-alkoxy species to *i*-alkoxy species, (d) deprotonation of *i*-alkoxy species, and (e) equilibration of *i*-hexene and *i*-hexane.

the mechanisms involved in this reaction is summarized in Fig. 16 [134, 135]. The amount of the noble metal, such as Pt, added is such that hexane/hexene equilibrium is established. Under the reaction conditions applied experimentally (230–250°C), this implies that the hexene/hexane ratio is about 10^{-6}, which suppresses undesirable deactivating oligomerization reactions. Hexene reacts readily with the zeolitic proton. An intermediate alkoxy species is formed, which can isomerize to the isoalkoxy, which upon deprotonation gives isoalkene. Isoalkene is subsequently hydrogenated to hexane.

It has been explained in a previous section that diffusion of hexane and isohexane can be considered to be fast. From a combination of theoretical and experimental data, a reaction energy scheme corresponding to the catalytic reaction cycle that converts *n*-hexene into *i*-hexene has been deduced. This is shown in Fig. 17 [136, 137]. As in Section V, adsorption on the siliceous part of the zeolite micropore is considered to be independent of proton activation.

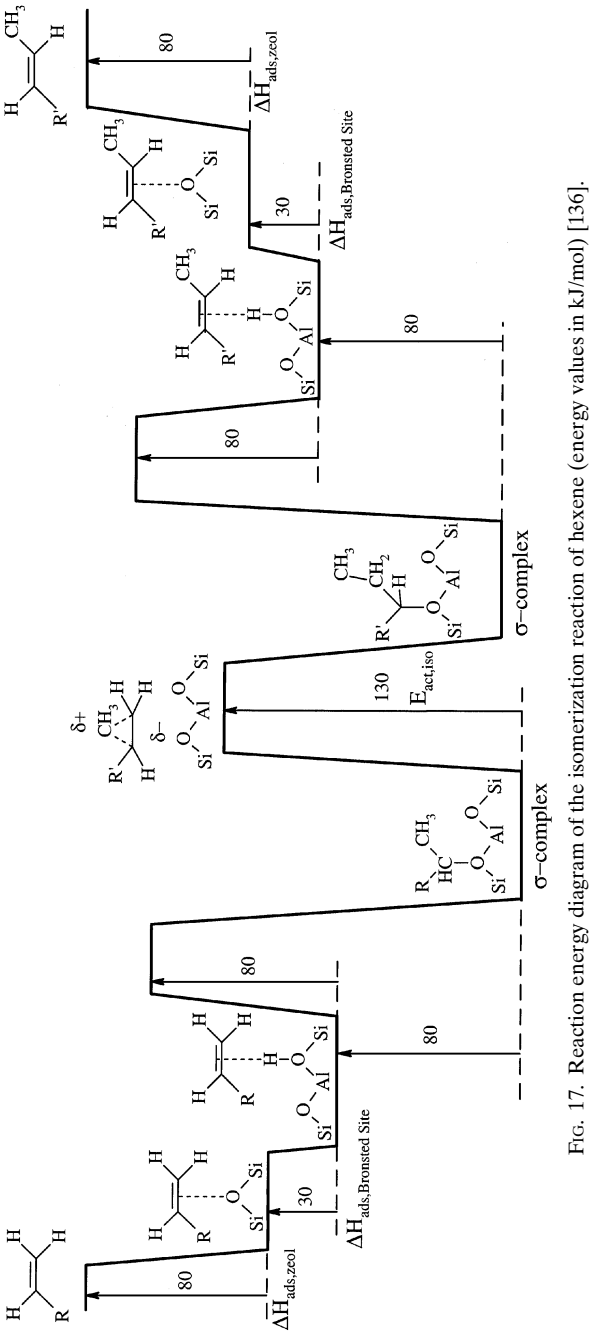

FIG. 17. Reaction energy diagram of the isomerization reaction of hexene (energy values in kJ/mol) [136].

Step 1 in the reaction energy diagram is the strongly micropore-dependent energy of adsorption of reactant hexene. In the diagram, the computed adsorption energy value in siliceous mordenite is used. The olefinic part of the molecule becomes π and, subsequently, σ coordinated in the subsequent steps. The best current estimation of the activation energy of the chemisorption reaction is ~60 kJ/mol (the cluster value, ~100 kJ/mol, corrected for by the screening contribution, ~40 kJ/mol). No accurate theoretical predictions of the activation energy of isomerization are yet available but experiment indicates that this value has to be between 120 and 140 kJ/mol [136–138]. As rate-limiting steps the rates of desorption and isomerization can compete. An estimate of preexponents is necessary to decide whether this is really the case.

We explained in Section IV. B that the positively charged transition states are stabilized by the interaction with the negatively charge zeolite wall. We also discussed the large entropy loss of adsorbed molecules compared to that in the gas phase. Hence, the transition state for the desorbing molecule will have a significantly larger entropy gain than occurs in proton activation. One may expect differences in the preexponent of $\sim 10^4$ [139]. Whereas this implies that for hexane isomerization the elementary rate constant of isomerization will be rate limiting, for larger molecules with higher adsorption energies, the rates of desorption and proton activation may compete. Under conditions where the rate of desorption is rate limiting, dynamic Monte Carlo simulations show that product molecules remain occluded in the one-dimensional channels. The micropore mouths become blocked by incoming molecules. As a consequence, the rate constant per proton decreases (see Fig. 18) [140].

In the absence of the need to include diffusion explicitly because it is fast, the kinetic equations for hexane isomerization reduce to classical steady-state expressions for the rate of isomerization:

$$r_{\text{iso}} = k_{\text{iso}} \cdot \Theta_{\text{alcoxy}} \tag{16a}$$

and

$$k_{\text{ads.alkene}} P_{\text{alkene}} \left(1 - \Theta_{\text{alkane}} - \Theta_{\text{alkane}} - \Theta_{\text{alkoxy}}\right) = k_{\text{des}} \Theta_{\text{alkene}} + k_{\text{isom}} \Theta_{\text{alkoxy}}. \tag{16b}$$

To deduce r_{iso}, the elementary rate constant of isomerization, k_{iso}, has been assumed to be rate limiting. The competition of protonic sites adsorption for alkane or alkene has been explicitly included in the kinetic scheme of reactions. Using available data on the adsorption isotherms of alkane and theoretical protonation energies, the elementary rate constant parameters of k_{iso} can be deduced from experiment by measuring the rate of isomerization

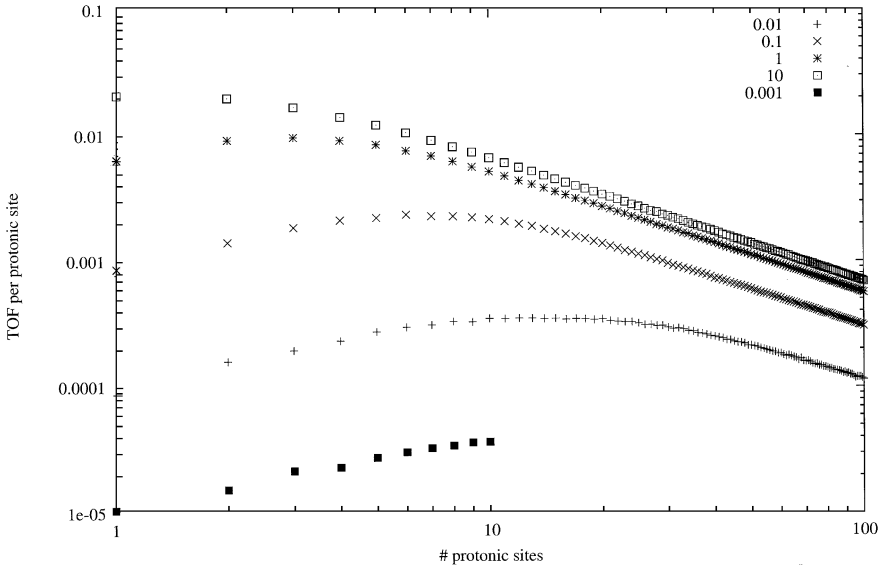

FIG. 18. Simulated turnover frequency as a function of the number of protonic sites. The loading is about 5%, every nine site can become a protonic site, and the rate constant for A → B transformation is 10, 1, 0.1, 0.01, and 0.001 times the rate constant for desorption from the top to the bottom curves [140].

as a function of the partial pressure of hexane [138]:

$$\frac{1}{r_{\text{iso}}} = a + \frac{b}{P_{\text{hexane}}}$$

$$\begin{cases} a = \dfrac{1}{k_{\text{iso}}} + \dfrac{P_{\text{H}_2}}{k_{\text{iso}} K_{\text{prot}}} \dfrac{K_{\text{ads,hexane}}}{K_{\text{ads,hexene}} K_{\text{dehydr}}} \\ b = \dfrac{P_{\text{H}_2}}{k_{\text{iso}} K_{\text{prot}} K_{\text{dehydr}} K_{\text{ads,hexene}}}. \end{cases}$$

Table V collects values for the activation energies of isomerization and protonation as deduced by De Gauw and van Santen [138] from kinetic measurements. A comparison of the turnover frequency per proton (TOF) and k_{iso} is made in Table V. One notes that the large differences in measured overall TOFs of different zeolites disappear for the elementary rate constant k_{iso}. This implies that the difference in apparent acidity of the zeolite is due mainly to the difference in adsorption isotherms of the different zeolites. One notes the small variation in activation and protonation energy values, which implies a slight dependence of protonation on the micropore channel size and dimension.

TABLE V
MEASURED VALUES OF THE HYDROISOMERIZATION REACTION OF HEXANE CATALYZED BY DIFFERENT ZEOLITES[a]

	ΔH_{prot}	E_{iso}^{act}	k_{iso}^{b}	TOF[b]
H-Beta	−46	145	$1.7 \cdot 10^{-2}$	$5.0 \cdot 10^{-3}$
H-Mordenite	−19	120	$2.7 \cdot 10^{-2}$	$1.1 \cdot 10^{-2}$
H-ZSM-5	−23	105	$2.8 \cdot 10^{-2}$	$4.1 \cdot 10^{-3}$
H-ZSM-22	−35	106	$1.7 \cdot 10^{-2}$	$1.6 \cdot 10^{-3}$

[a] The values are the enthalpies of protonation (ΔH_{prot}; kJ/mol), the activation energies of the isomerization reaction (E_{iso}^{act}; kJ/mol), the rate constants of isomerization (k_{iso}; s^{-1}), and the turnover frequencies (TOF; s^{-1}) [139].
[b] Measured at 240°C.

V. Concluding Remarks

The aim of this paper has been to present an overview of the current status of atomistic simulations in relation to an understanding or prediction of zeolite catalyst performance. In the initial sections, we have described that the attractive van der Waals and the repulsive Born interactions determine micropore size- and shape-dependent differences between different zeolite structures. This affects overall catalytic rates because it controls the degree of micropore filling under catalytic conditions.

The discussion of reactivity focused on the activation of hydrocarbons by zeolitic protons. The deprotonation energy of a proton is weakly dependent on the zeolite crystallographic position but may be strongly zeolite composition dependent, especially at high concentrations of three valent cations (Al, Ga) in the zeolite framework. Nonetheless, the deprotonation energy is a local property of the OH bond, which can be estimated using quantum-chemical calculations by extrapolation from properly terminated cluster calculations.

The elementary rate constant for proton activation is weakly dependent on the micropore size as long as steric constraints do not affect the transition state. Because of the zwitterionic nature of the transition state, dielectric screening by the oxygen atoms of the micropore tends to decrease the cluster-calculated transition state energies to 10 to 30% of the activation energies. Steric constraints on the transition state may substantially increase the cluster-computed activation energies by similar amounts. These steric constraints can be computed from periodical DFT calculations or from transition-state model structures using Monte Carlo adsorbate–zeolite pore interaction calculations.

The overall concept that appears central is that zeolite activity depends on two energy terms: the energy of adsorption, controlled by the micropore size-dependent van der Waals forces; and the protonation energy, which is a local property usually rather independent of the micropore size, unless steric constraints limit optional interactions between proton and substrate.

The activation energy for proton transfer can be viewed as a lattice oxygen Lewis-base and proton Brønsted-acid synergetic event [3]. One generally finds that activation energies of proton-activated reactions are rather high: between 100 and 200 kJ/mol for proton-activated elementary reaction steps in hydrocarbon conversion catalysis. This is the main reason for the relatively low TOF per proton ($\sim 10^2\ s^{-1}$) for this type of reaction. Similarly to enzymes [31], the weak van der Waals-type interaction determines the size- and shape-dependent behavior.

REFERENCES

1. Catlow, C. R. A, Cormack, A. N., and Theobald, F., *Acta Crystallogr. B* **40,** 195 (1984).
2. Catlow, C. R. A., Ackermann, L., Bell, R. G., Corà, F., Gay, D. H., Nygren, M. A., Pereira, J. C., Sastre, G., Slater, B., and Sinclair, P. E., *Faraday Discuss.* **106,** 1 (1997).
3. van Santen, R. A., and Kramer, G. J., *Chem. Rev.* **95,** 637 (1995).
4. Sauer, J., in *Modeling of Structure and Reactivity in Zeolites* (Catlow, C. R. A., ed.), Academic Press, London, 1992, p. 183.
5. Sauer, J., in *Cluster Models for Surface and Bulk Phenomena: Proceedings of a NATO Advanced Research Workshop* (Pacchioni, G., Bagus, P. S., and Parmigiani, F., eds.), Plenum Press, London, 1992, p. 533.
6. van Santen, R. A., De Bruyn, D. P., Den Ouden, C. J. J., and Smit, B., in *Introduction to Zeolite Science and Practice* (Van Bekkum, H., Flaningen, E. M., and Jansen, J. C., eds.), Elsevier, Amsterdam, 1991, Vol. 58, p. 317.
7. Corma, A., Llopis, F., Viruela, P., and Zicovich-Wilson, C., *J. Am. Chem. Soc.* **116,** 134 (1994).
8. Sauer, J., Ugliengo, P., Garrone, E., and Saunders, V. R., *Chem. Rev.* **94,** 2095 (1994).
9. Nicholas, J. B., *Topics Catal.* **4,** 157 (1997).
10. Civalleri, B., Zicovich-Wilson, C. M., Ugliengo, P., Saunders, V. R., and Dosevi, R., *Chem. Phys. Lett.* **292,** 394 (1998).
11. Brändel, M., and Sauer, J., *J. Am. Chem. Soc.* **120,** 1556 (1998).
12. Jeanvoine, Y., Ángyán, J. G., Kresse, G., and Hafner, J., *J. Phys. Chem. B* **102,** 5573 (1998).
13. Blaszkowski, S. R., and van Santen, R. A., in *Transition State Modeling for Catalysis* (Truhlar, D. G., and Morokuma, K., eds.), ACS Symposium Series 721, Am. Chem. Soc., 19xx, Chap. 24
14. Beck, L. W., Xu, T., Nicholas, J. B., and Haw, J. F., *J. Am. Chem. Soc.* **117,** 11594 (1995).
15. Corma, A., Sastre, G., and Viruela, P. M., *J. Mol. Catal. A* **100,** 75 (1995).
16. Saintigny, X., van Santen, R. A., Clémendot, S., and Hutschka, F., *J. Catal.* **183,** 107 (1999).
17. Frash, M. V., and van Santen, R. A., *Topics Catal.* **9,** 191 (1999).
18. Kazansky, V. B., *Catal. Today* **51,** 419 (1999).

19. Boronat, M., Viruela, P., and Corma, A., *J. Phys. Chem. A* **102,** 982 (1998).
20. Evleth, E. M., Kassab, E., Jessrich, H., Allavena, M., Montero, L., and Sierra, L. R., *J. Phys. Chem.* **100,** 11368 (1996).
21. Esteves, P. M., Nascimento, M. A. C., and Mota, C. J. A., *J. Phys. Chem. B* **103,** 10417 (1999).
22. Frash, M. V., Kazansky, V. B., Rigby, A. M., and van Santen, R. A., *J. Phys. Chem. B* **101,** 5346 (1997).
23. Sauer, J., Horn, H., Häser, M., and Ahlrichs, R., *Chem. Phys. Lett.* **173,** 26 (1990).
24. Blaszkowski, S. R., and van Santen, R. A., *J. Am. Chem. Soc.* **118,** 5152 (1996).
25. Blaszkowski, S. R., and van Santen, R. A., *J. Am. Chem. Soc.* **119,** 5020 (1997).
26. Sierra, L. R., Kassab, E., and Evleth, E. M., *J. Phys. Chem.* **97,** 641 (1993).
27. Yoshizawa, K., Shiota, Y., Yumura, T., and Yamabe, T., *J. Phys. Chem. B* **104,** 734 (2000).
28. Barbosa, L. A. M. M., and van Santen, R. A., *J. Mol. Catal. A* **166**(1), 101 (2001).
29. Rice, M. J., Chakraborty, A. K., and Bell, A. T., *J. Phys. Chem. A* **102,** 7498 (1998).
30. Fois, E., Gamba, A., and Tabachi, G., *Phys. Chem. Chem. Phys.* **1,** 531 (1999).
31. Barbosa, L. A. M. M., and van Santen, R. A., *J. Catal.* **191,** 200 (2000).
32. Frenkel, D., and Smit, B., in *Understanding Molecular Simulation: From Algorithms to Applications,* Academic Press, San Diego, 1996.
33. Bates, S. P., and van Santen, R. A., *Adv. Catal.* **42,** 1 (1998).
34. Bell, A. T., Maginn, E. J., and Theodorou, D. N., in *Handbook of Heterogeneous Catalysis* (Ertl, G., Knözinger, H., and Weitkamp, J., eds.), Wiley–VCH, Weihheim, Germany, 1997, Vol. 3, p. 1165.
35. Kramers, H. A., *Physica* **7,** 284 (1940).
36. Gilbert, R. G., and Smith, S. C., *Theory of Unimolecular and Recombination Reactions,* Blackwell, Oxford, 1990.
37. van Santen, R. A., and Niemantsverdriet, J. W., *Chemical Kinetics and Catalysis,* Plenum, New York, 1995.
38. Schleyer, P. v. R. (ed.), in *Encydopedia of Computational Chemistry,* John Wiley & Sons, New York, 1998.
39. Bernardi, F., and Robb, M. A., in *Ab Initio Methods in Quantum Chemistry—I* (Lawley, K. P., ed.), John Wiley & Sons, New York, 1987, p. 155.
40. Venuto, P. B., *Microporous Matter* **2,** 297 (1994).
41. Hölderich, W. F., and Van Bekkum, H., in *Introduction to Zeolite Science and Practice* (Van Bekkum, H., Flaningen, E. M., and Jansen, J. C., eds.), Elsevier, Amsterdam, 1991, Vol. 58, p. 631 .
42. Nicholas, J. B., *Topics Catal.* **4,** 157 (1997).
43. Rigby, A. M., Kramer, G. J., and van Santen, R. A., *J. Catal.* **170,** 1 (1997).
44. Koller, H., Engelhardt, G., and van Santen, R. A., *Topics Catal.* **9,** 163 (1999).
45. van Santen, R. A., *Catal. Today* **38,** 377 (1997).
46. Olah, G. A., and Donovan, D. J., *J. Am. Chem. Soc.* **99,** 5026 (1977).
47. Olah, G. A., Prakash, G. K. S., and Sommer, J., in *Superacids,* Wiley Interscience, New York, 1985.
48. Olah, G. A., Prakash, G. K. S., Williams, R. E., Field, L. D., and Wade, K., in *Hypercarbon Chemistry,* Wiley Interscience, New York, 1987.
49. De Man, A. J. M., Van Beest, B. W. H., Leslie, M., and van Santen, R. A., *J. Phys. Chem.* **94,** 2524 (1990).
50. Schröder, K.-P., and Sauer, J., *J. Phys. Chem.* **100,** 11043 (1996).
51. Levien, L., Previtt, C. T., and Weider, D. J., *Am. Mineral.* **65,** 925 (1980).
52. De Man, A. J. M., and van Santen, R. A., *Zeolites* **12,** 269 (1992).
53. Lee, C., Parrillo, D. J., Gorte, R. J., and Farneth, W. E., *J. Am. Chem. Soc.* **118,** 3262 (1996).

54. Gorte, R. J., *Catal. Lett.* **62,** 1 (1999).
55. Bezuz, A. G., Kiselev, A. G., Lopatkin, A. A., and Quang Du, P., *J. Chem. Soc. Faraday Trans. II* **74,** 367 (1978).
56. Kiselev, A. A., and Quang Du, P., *J. Chem. Soc. Faraday Trans. II* **77,** 17 (1981).
57. Bezuz, A. Z., Kocirik, M, Kiselev, A. V., Lopatkin, A. A., and Vasilyena, E. A., *Zeolites* **6,** 101 (1986).
58. Meinander, N., and Tabisz, G. C., *J. Chem. Phys.* **79,** 416 (1983).
59. Bell, R. G., Lewis, D. W., Voigt, P., Freeman, C. M., Thomas, J. M., and Catlow, C. R. A., in *Proceedings of the 10th International Conference, Garmisch-Partenkirchen, 1994* (Weitkamp, J., Karge, H. G., Pfeifer, H., and Hölderich, W., eds.), Elsevier, Amsterdam, 1994, Part C, p. 2075.
60. Kristyan, S., and Pulay, P., *Chem. Phys. Lett.* **229,** 175 (1994).
61. Pelmenschikov, A., and Leszcynski, J., *J. Phys. Chem. B* **103,** 6886 (1999).
62. Allen, M. P., and Tildesley, D. J., in *Computer Simulation of Liquids,* Oxford Science, Oxford, 1987.
63. Frenkel, D., in *Proceeding of the Euroconference on Computer Simulation in Condensed Matter Physics and Chemistry, Como, 1995* (Binder, K., and Ciccotti, G., eds.), Italian Physical Society, Bolognia, 1995, Chap. 7.
64. Smit, B., and Siepmann, J. I., *J. Chem. Phys.* **98,** 8442 (1994).
65. Smit, B., *Mol. Phys.* **85,** 153 (1995).
66. June, R. L., Bell, A. T., and Theodorou, D. N., *J. Phys. Chem.* **96,** 1051 (1992).
67. Smit, B., and Maesen, T. L. M., *Nature* **374,** 42 (1995).
68. Kiselev, A. V., and Quang Du, P., *J. Chem. Soc. Faraday Trans.* **77,** 1 (1981).
69. Freeman, C. M., Catlow, C. R. A., Thomas, J. M., and Brode, S., *Chem. Phys. Lett.* **186,** 137 (1991).
70. Bates, S. P., Van Well, W. J. M., van Santen, R. A., and Smit, B., *J. Am. Chem. Soc.* **118,** 6753 (1996).
71. Bates, S. P., Van Well, W. J. M., van Santen, R. A., and Smit, B., *J. Phys. Chem.* **100,** 17573 (1996).
72. Smit, B., and Maesen, T. L. M., *Nature* **374,** 42 (1995).
73. Van Well, W. J. M., Cottin, X., and Smit, B., *J. Am. Chem. Soc.* **37,** 1081 (1998).
74. Schumacher, R., and van Santen, R. A., in preparation.
75. Eder, F., Ph.D. thesis, TU, Twente, 1996.
76. Denayer, J. F., Baron, G. V., Martens, J. A., and Jacobs, P. A., *J. Phys. Chem. B* **102,** 3077 (1998).
77. Noordhoek, N. J., Van Ijzendoorn, L. J., Anderson, B. A., De Gauw, F. J., van Santen, R. A., and De Voigt, M. J., *Ind. Eng. Chem. Res.* **37,** 825 (1998).
78. Schuring, D., Jansen, A. P. J., and van Santen, R. A., *J. Phys. Chem. B* **104,** 941 (2000).
79. Clark, L. A., Ye, G. T., Gupta, A., Hall, L. L., and Snurr, R. O., *J. Chem. Phys.* **111,** 1209 (1999).
80. Heink, W., Kärger, J., Pfeifer, H., and Stallmach, F. J. M. M., *J. Am. Chem. Soc.* **112,** 2175 (1990).
81. Kärger, J., and Rutheven, D. M., in *Diffusion in Zeolites and Other Microporous Solids,* Wiley–Interscience, New York, 1992.
82. Callaghan, P. T., in *Principles of Nudear Magnetic Resonance Microscopy,* Clarendon, Oxford, 1991.
83. Hong, U., Kärger, J., and Pfeifer, H., *J. Am. Chem. Soc.* **113,** 4812 (1991).
84. Kärger, J., and Pfeifer, H., in *NMR Techniques in Catalysis* (Bell, A. T., and Pines, A., eds.), Marcel Dekker, New York, 1994, p. 69.
85. Yashonath, S., and Santikary, P., *Mol. Phys.* **78,** 1 (1993).

86. Yashonath, S., and Santikary, P., *J. Chem. Phys.* **100,** 4013 (1994).
87. Yashonath, S., and Santikary, P., *J. Phys. Chem.* **97,** 3849 (1993).
88. Smit, B., Loyens, L. D. J. C., and Verbist, G. L. M. M., *Faraday Discuss.* **106,** 93 (1997).
89. Karpinski, Z., Gandhi, S. N., and Sachtler, W. M. H., *J. Catal.* **141,** 337 (1993).
90. Fraenkel, D., and Levy, M., *J. Catal.* **118,** 10 (1989).
91. Hinderen, J., and Keil, F., *J. Chem. Eng. Sci.* **51,** 2667 (1996).
92. Olah, G. A., and Schosberg, R. H., *J. Am. Chem. Soc.* **90,** 2726 (1968).
93. (a) Haw, J. F., Richardson, B. R., Oshiro, I. S., Lazo, N. D., and Speed, J. A., *J. Am. Chem. Soc.* **111,** 2052 (1989). (b) Haw, J. F., Nicholas, J. B., Xu, T., Beck, L. W., and Ferguson, D. B., *Acc. Chem. Res.* **29,** 259 (1996).
94. Haag, W. O., and Dessau, R. M., in *Proce. 8th Int. Congr. Catal.,* Berlin, 1984, Vol. 2, p. 305.
95. Mikheikin, I. D., Senchenya, I. N., Lumpov, A. I., Zhidomirov, G. M., and Kazansky, V. B., *Kinet. Katal.* **20,** 496 (1979).
96. Lumpov, A. I., Mikheikin, I. D., Zhidomirov, G. M., and Kazansky, V. B., *Kinet. Katal.* **20,** 1979 (1979).
97. Senchenya, I. N., Mikheikin, I. D., Zhidomirov, G. M., and Kazansky, V. B., *Kinet. Katal.* **22,** 1174 (1980).
98. Senchenya, I. N., Mikheikin, I. D., Zhidomirov, G. M., and Kazansky, V. B., *Kinet. Katal.* **21,** 1184 (1980).
99. Senchenya, I. N., Mikheikin, I. D., Zhidomirov, G. M., and Kazansky, V. B., *Kinet. Katal.* **23,** 591 (1982).
100. McVicker, G. B., Kramer, G. M., and Ziemiak, J. J., *J. Catal.* **83,** 286 (1983).
101. Bordiga, S., Civalleri, B., Spoto, G., Pazè, C., Lamberti, C., Ugliengo, P., and Zecchina, A., *Chem. Soc. Faraday Trans.* **21,** 3893 (1997).
102. Rozanska, X., van Santen, R. A., Hutscka, F., and Hafner, J., unpublished results.
103. Kazansky, V. B., and Senchenya, I. N., *J. Catal.* **119,** 108 (1989).
104. Kramer, G. J., van Santen, R. A., Emeis, C. A., and Nowak, A. K., *Nature* **363,** 529 (1993).
105. Koller, H., Meijer, E. L., and van Santen, R. A., *Solid State Nucl. Magn. Res.* **9,** 165 (1997).
106. Parr, R. G., and Yang, W., in *Density-Functional Theory of Atoms and Molecules,* Oxford University, New York, 1989.
107. Ziegler, T., *Chem. Rev.* **91,** 651 (1991).
108. Labonowski, J. K., and Andzelm, J. W. (eds.), in *Density Functional Methods in Chemistry,* Springer, Berlin, 1991.
109. Krossner, M., and Sauer, J., *J. Phys. Chem.* **100,** 6199 (1996).
110. (a) Haase, F., and Sauer, J., *J. Am. Chem. Soc.* **117,** 3780 (1995). (b) Moravetski, V., Hill, J., Eichler, U., Cheetman A. K., and Sauer, J., *J. Am. Chem. Soc.* **118,** 13015 (1996).
111. Schröder, K.-P., Sauer, J., Leslie, M., Catlow, C. R. A., and Thomas, J. M., *Chem. Phys. Lett.* **188,** 320 (1992).
112. Sauer, J., Eichler, U., Meier, U., Schäfer, A., von Arnim, M., and Ahlrichs, R., *Chem. Phys. Lett.* **308,** 147 (1999).
113. Brand, H. V., Curtiss, L. A., and Iton, L. E., *J. Phys. Chem.* **96,** 7725 (1992).
114. Zygmunt, S. A., Curtiss, L. A., Iton, L. E., and Erhardt, M. K., *J. Phys. Chem.* **100,** 6663 (1996).
115. Brand, H. V., Curtiss, L. A., and Iton, L. E., *J. Phys. Chem.* **97,** 12773 (1993).
116. Ugliengo, P., Ferrari, A. M., Zecchina, A., and Garrone, E., *J. Phys. Chem.* **100,** 3632 (1996).
117. Civalleri, B., Garrone, E., and Ugliengo, P., *J. Phys. Chem. B* **102,** 2373 (1998).
118. Frash, M. V., Makarova, M. A., and Rigby, A. M., *J. Phys. Chem. B* **101,** 2116 (1997).
119. Bonn, M., Bakker, H. J., Domen, K., Hirose, C., Kleyn, A. W., and van Santen, R. A., *Catal. Rev. Sci. Eng.* **40,** 127 (1998).

120. Haase, F., Sauer, J., and Hutter, J., *J. Chem. Phys. Lett.* **266,** 397 (1997).
121. Boronat, M., Zicovich-Wilson, C. M., Corma, A., and Viruela, P., *Phys. Chem. Chem. Phys.* **1,** 537 (1999).
122. Rozanska, X., van Santen, R. A., Hutschka, F., and Hafner, J., *J. Am. Chem. Soc.* **123,** (2001).
123. Sinclair, P. E., De Vries, A., Sherwood, P., Catlow, C. R. A., and van Santen, R. A., *J. Chem. Soc. Faraday Trans.* **94,** 3401 (1998).
124. Greatbanks, S. P., Hillier, I. H., and Sherwood, P., *J. Comp. Chem.* **18,** 562 (1997).
125. Sherwood, P., De Vries, A. H., Collins, S. J., Greatbanks, S. P., Burton, S. A., Vincent, M. A., and Hillier, I. H., *Faraday Discuss.* **106,** 79 (1997).
126. De Vries, A. H., Sherwood, P., Collins, S. J., Rigby, A. M., Rigutto, M., and Kramer, G. J., *J. Phys. Chem. B* **103,** 6133 (1999).
127. Gao, J., in *Reviews in Computational Chemistry* (Lipkowitz, K. B., and Boyd, D. B., eds.), VCH, New York, 1996, Vol. 7.
128. Pisani, C., and Birkenheuer, U., *Int. J. Quant. Chem.* **29,** 221 (1995).
129. Parsons, D., Ángyán, J. G., and Hafner, J., in preparation.
130. Klein, H., Kirschhoch, C., and Fuess, H., *J. Phys. Chem.* **98,** 12345 (1994).
131. Vos, A., Rozanska, X., Schoonheydt, R. A., van Santen, R. A., Hutschka, F., and Hafner, J., *J. Am. Chem. Soc.* **123,** 2799 (2001).
132. Kazansky, V. B., Frash, V. B., and van Santen, R. A., *Catal. Lett.* **48,** 61 (1997).
133. Kazansky, V. B., Frash, V. B., and van Santen, R. A., *Stud. Surf. Sci. Catal.* **105,** 2283 (1997).
134. Weisz, P. B., in *Advances in Catalysis and Related Subjects.* (Eley, D. D., Selwood, P. W., and Weisz, P. B., eds.), Academic Press, London, 1963, Vol. 13, p. 157.
135. Maxwell, I. E., and Stork, W. H. J., in *Introduction to Zeolite Science and Practice* (Van Bekkum, H., Flaningen, E. M., and Jansen, J. C., eds.), Elsevier, Amsterdam, 1991, Vol. 58, p. 571.
136. Van de Runstraat, A., Van Grondelle, J., and van Santen, R. A., *Ind. Eng. Chem. Res.* **36,** 3116 (1997).
137. Van de Runstraat, A., Kamp., J. A., Stobbelaar, P. J., Van Grondelle, J., Krijnen, S., and van Santen, R. A., *J. Catal.* **171,** 77 (1997).
138. De Gauw, F. J. M. M., and van Santen, R. A., in preparation.
139. van Santen, R. A., and Niemantsverdriet, J. W., in *Chemical Kinetics and Catalysis,* Plenum, New York, 1995, p. 159.
140. Jansen, A. P. J., unpublished results.